Polyamorphism in a metallic glass

H. W. SHENG[1]*, H. Z. LIU[2,3], Y. Q. CHENG[1], J. WEN[4], P. L. LEE[5], W. K. LUO[1], S. D. SHASTRI[5] AND E. MA[1]*

[1]Department of Materials Science and Engineering, Johns Hopkins University, Baltimore, Maryland 21218, USA
[2]HPCAT, Geophysical Laboratory, Carnegie Institution of Washington, Building 434E, 9700 South Cass Avenue, Argonne, Illinois 60439, USA
[3]Center for the Condensed Matter Science and Technology, Harbin Institute of Technology, Harbin 150080, China
[4]Institute of Metal Research, Chinese Academy of Sciences, 72 Wenhua Road, Shenyang 110016, China
[5]XOR, Advanced Photon Source, Argonne National Laboratory, Argonne, Illinois 60439, USA
*e-mail: hwsheng@jhu.edu; ema@jhu.edu

Published online: 18 February 2007; doi:10.1038/nmat1839

A metal, or an alloy, can often exist in more than one crystal structure. The face-centred-cubic and body-centred-cubic forms of iron (or steel) are a familiar example of such polymorphism. When metallic materials are made in the amorphous form, is a parallel 'polyamorphism' possible? So far, polyamorphic phase transitions[1–7] in the glassy state have been observed only in glasses involving directional and open (such as tetrahedral[4,5]) coordination environments. Here, we report an *in situ* X-ray diffraction observation of a pressure-induced transition between two distinct amorphous polymorphs in a $Ce_{55}Al_{45}$ metallic glass. The large density difference observed between the two polyamorphs is attributed to their different electronic and atomic structures, in particular the bond shortening revealed by *ab initio* modelling of the effects of *f*-electron delocalization[8–10]. This discovery offers a new perspective of the amorphous state of metals, and has implications for understanding the structure, evolution and properties of metallic glasses and related liquids. Our work also opens a new avenue towards technologically useful amorphous alloys that are compositionally identical but with different thermodynamic, functional and rheological properties[11] due to different bonding and structural characteristics.

Polyamorphism[1,11], the amorphous analogue of the well-known crystalline polymorphism[12], refers to the transition between different and distinct amorphous states (phases), where density, at a fixed composition, is usually the order parameter. For glasses, hydrostatic pressure is usually the thermodynamic variable used to induce polyamorphism[1–7]. Perhaps not surprisingly, all of the materials reported to exhibit polyamorphism in the glassy state, such as amorphous ice[2], silica[3], silicon[4,5] and chalcogenide glasses[6], although having different characters in bonding, all tend to involve directional coordination. This leads to an open local environment that, under hydrostatic pressure, switches to a more densely packed structure[4,5]. Thermodynamically, such polymorphic phase changes are often first-order transitions[6,7,13]. However, under pressure and at low temperatures, the transition can be sluggish and hysteretic owing to kinetic reasons[3,5,13]. From the perspective of an energy landscape, polyamorphism may be attributed to visitations to distinct megabasins on the potential-energy surface[14].

Metallic glasses (MGs) including 'bulk MGs' are newcomers to the glass family[15]. They are distinctly different from the traditional network-forming glasses, as they have metallic bonds that are non-directional in nature. This invites the question: would polyamorphism ever occur in MGs? At first glance, it is tempting to dismiss this possibility, because the as-prepared MGs are already spatially compact. Indeed, the density increase under pressure has been found to be gradual and completely reversible, as judged from X-ray diffraction (XRD) patterns (one example is shown in Supplementary Material, Fig. S1)[16,17]. However, a qualitative and abrupt change in electronic structure and bonding, an important origin for polyamorphism, remains unexplored for metallic liquids and glasses. Here, we report the behaviour of amorphous $Ce_{55}Al_{45}$, prepared using melt spinning (see the Methods section and Supplementary Information, Fig. S2). In its crystalline form, Ce is known to exhibit polymorphic transitions starting from rather low pressures due to its strongly correlated 4*f*-electrons and their delocalization[8–10], with large density changes[18]. For the melting transition of Ce, the slope of the coexistence line in pressure–temperature (P–T) space is negative[19].

Figure 1 shows synchrotron XRD patterns (see the Methods section for details) of the $Ce_{55}Al_{45}$MG, obtained *in situ* as a function of hydrostatic pressure. With increasing pressure, the first sharp diffraction peak shifts to higher momentum transfer, q, see Fig. 1a. This shift proceeds at a relatively fast pace over the pressure range of 2–13 GPa (see Fig. 1c). Accompanying this, the diffraction intensity maxima between 3 and 4 $Å^{-1}$ diminished, whereas those between 4 and 5.5 $Å^{-1}$ intensified. The final XRD features at 30 GPa are obviously different from those at ambient pressure (see more detailed analysis below). This is the first sign that a different amorphous phase has resulted. No crystallization was observed from carefully inspecting the two-dimensional XRD patterns recorded on the image plate.

Figure 1b shows the unloading process. There also seems to be two regimes for the shift of the first peak. The gradual move to lower q is slow over a wide range of pressure, and only accelerates to a rapid pace in the last stage of decompression, as marked in Fig. 1d. The same also happens for the features between 3 and 6 $Å^{-1}$, which evolved in the direction reversing the changes during compression. Moreover, by comparing the XRD patterns at a given pressure during the loading and unloading processes (see below), it is obvious that decompression did not re-trace the behaviour during the compression, for a wide range of pressures. This is quite different from the observation for other MGs, for example, Supplementary Information, Fig. S1, and the hysteresis is reminiscent of that observed in polyamorphic transitions[3,5]. On decompression back to ambient pressure, the first peak finally approached its original position before compression.

©2007 Nature Publishing Group

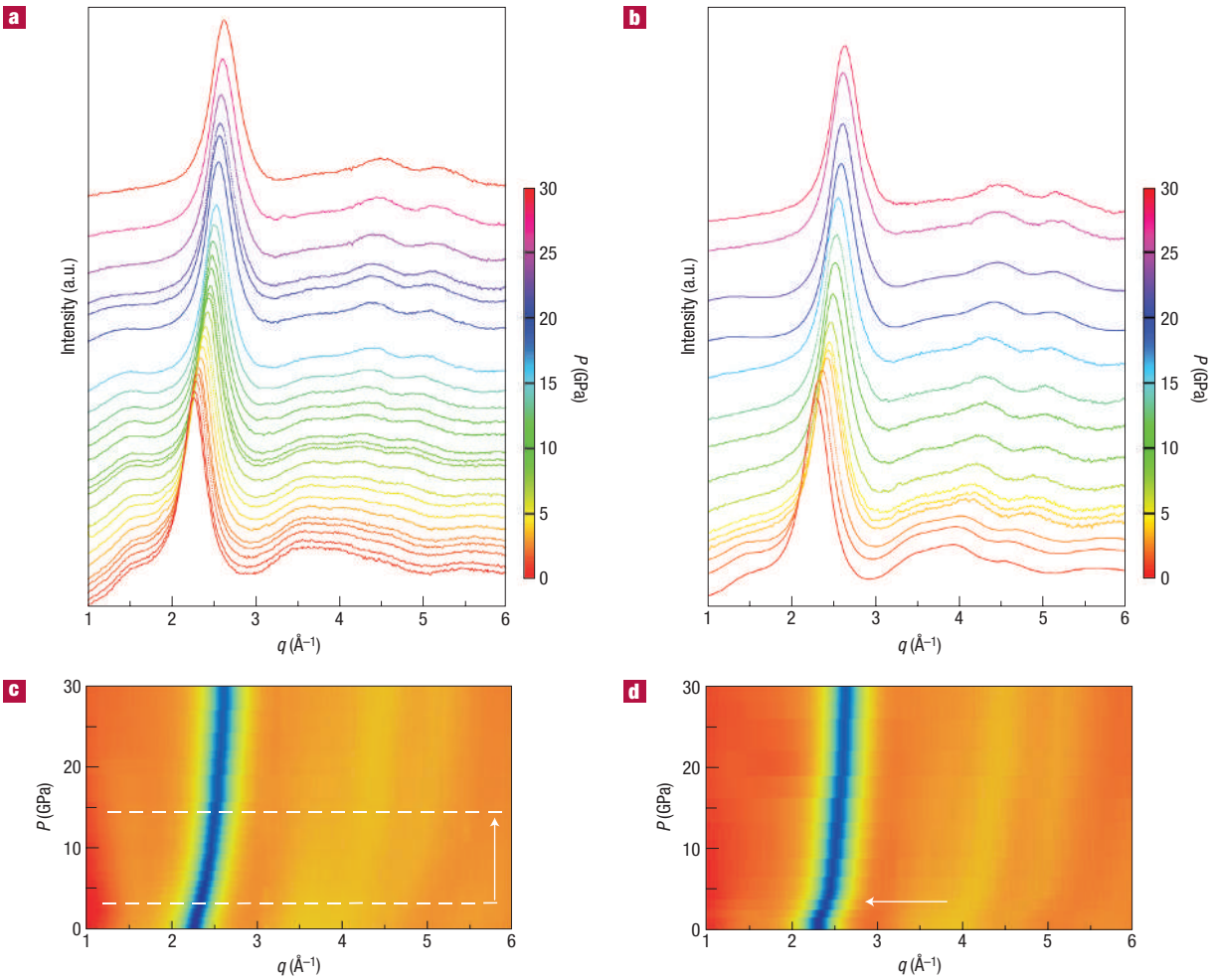

Figure 1 XRD patterns of the $Ce_{55}Al_{45}$ metallic glass in a diamond anvil cell. a,**b**, XRD patterns obtained *in situ* during the compression (**a**) and decompression (**b**) experiments. **c**,**d**, The different behaviours of the XRD intensity peak shift with pressure: the arrow in **c** illustrates a gradual movement during compression in the pressure range from 2.0 to 13.5 GPa (marked with dashed lines), whereas the arrow in **d** marks the abrupt shift towards lower q, at around 2 GPa during decompression.

Essentially the same trends and conclusions were obtained in analysing the structure factors derived from the XRD patterns, see Supplementary Information, Fig. S3.

The XRD peak positions reflect changes in atomic density, so it would be instructive to convert Fig. 1 into a plot of specific volume versus pressure, see Fig. 2. The density of the glass was determined using simulations (see the Methods section) rather than by estimating using the position of the first peak alone[3,7]. In Fig. 2, we again observe a fast decrease of the average atomic volume (corresponding to the density increase, as well as the shift of XRD peaks towards higher q in Fig. 1) with increasing pressure. Interestingly, the volume decrease did not follow the pressure–volume (P–V) equation of state (EOS) predicted for this $Ce_{55}Al_{45}$ glass, upper line in Fig. 2. This prediction was made using *ab initio* calculations for the glass at room temperature, assuming that the Ce f-electron is localized following the local density approximation LDA+U model (where U is the Hubbard term) used for crystalline Ce (see the Methods section and Supplementary Information, Fig. S4). Note that the calculated volume (or density), as well as the structural features (see Supplementary Information, Fig. S5), is in good agreement with that of the experimental sample at ambient pressure (point A in Fig. 2). As seen in Fig. 2, the volume decrease with pressure begins to exhibit an obvious deviation from the predicted curve at $P > 2$ GPa. The decrease is at such a pace that at 13.5 GPa the volume in fact coincides with that expected for the same glass when all of the f-electrons are delocalized (lower curve, see the Methods section and Supplementary Information, Fig. S4). Above this pressure, the P–V behaviour is in agreement with the EOS prediction assuming delocalized f-electrons.

These results suggest that we have observed a polyamorphic transition of the Ce–Al glass from a low-density state into a high-density state (the density difference between the two states is as large as 14% at ambient pressure, see Fig. 2). On decompression, the volume closely follows the prediction for the high-density phase, suggesting that the f-electrons remained largely delocalized, until the pressure approached 2 GPa, around which a rapid return to the low-density phase set in. To make sure that the data are reproducible and sufficient data points are collected to substantiate the conclusions, four different samples were studied in four separate XRD runs at different times at the Advanced Photon Source. These results are summarized using different symbols in Fig. 2. It can be seen that the data sets are consistent with one another. In all cases, the density after decompression back to ambient pressure approached the original one, which is unlikely if

©2007 Nature Publishing Group

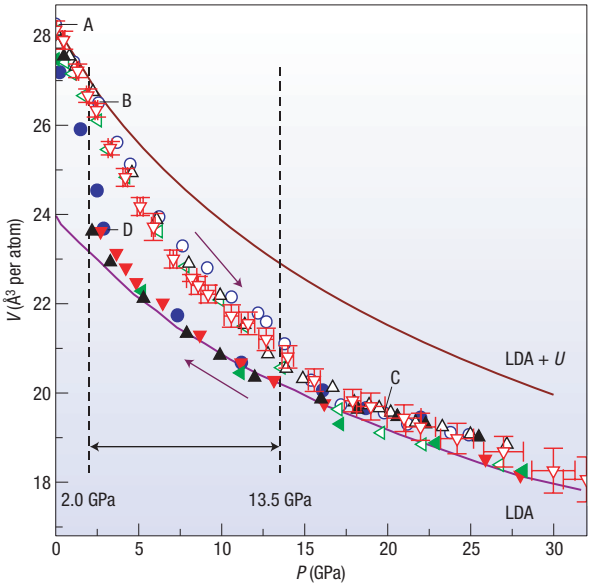

Figure 2 Specific volume versus pressure for amorphous $Ce_{55}Al_{45}$. Four different symbols represent four different *in situ* XRD runs on four different samples. The open symbols are for compression, and the solid symbols are for decompression. The EOS predicted using first-principles calculations for different *f*-electron behaviours are also shown: the upper line is for the case of localized 4*f*-electrons from the LDA + *U* calculation, and the lower line is from the LDA calculation assuming 4*f* delocalization. For clarity, errors bars are shown only for one set of the data. The vertical error bars represent the accuracy of density (specific volume) determined using our modelling techniques. The horizontal error bars account for the small pressure variation during the experiment (before and after the XRD run). See the text for discussions of points A–D. Note the abrupt transition during decomposition.

crystallization occurred. For all four data sets, the decompression data points below 13.5 GPa did not re-trace the compression ones. Taken together, the information in Fig. 2 clearly demonstrates that there are two amorphous phases with a large density disparity, governed by two different equations of state, and the transition between the low-density and high-density states is hysteretic.

Next, we analyse the structure factors to further demonstrate that the two amorphous phases are structurally distinct and correspond to the low-density and high-density forms modelled using the *f*-electron localization/delocalization assumptions. Figure 3 directly compares the XRD structure factor of the two glass forms during compression (Fig. 3a) and during decompression (Fig. 3c), at about the same pressure. Specifically, we compare the glass at 2.6 GPa during compression, when the glass is still very close to the low-density form (point B in Fig. 2), and that at 2.9 GPa during decompression (point D in Fig. 2), where the alloy is mostly in its high-density state before an abrupt density drop that is soon to begin. Clearly, the first peak positions are different, and the rest of the features are also distinctly different (see also the direct superposition in Supplementary Information, Fig. S3c). Moreover, the same figures show that these experimental structure factors agree quite well with those calculated for the low-density and high-density glasses that have different electronic and atomic structures. The structure factor calculations were made possible by using relatively large systems (100,000 atoms) simulated using effective atomic potentials derived from *ab initio* results using the inverse Monte Carlo (IMC) simulation method[20] (see explanations in Supplementary Information, Fig. S5 for this structural modelling of point A in Fig. 2), see Fig. 3b,d. Meanwhile, the simulated systems allow the extraction of the partial pair distribution functions, which are also compared for the two glass states (see Fig. 3b versus d), and other atomic packing details. These figures are strongly suggestive of electronic and atomic structural differences between the two amorphous phases. For the high-density state (Fig. 3d), the Ce–Ce effective interatomic potential derived exhibits a double-well (shell) feature, and correspondingly there are two Ce–Ce nearest-neighbour coordination peaks (shells), one of which has a much shortened bond length. The short-range atomic structure changed accordingly. The nearest-neighbour coordination numbers for Al and Ce (see Fig. 3d) are 12.3 (4.5 Al + 7.8 Ce) and 13.6 (6.1 Al + 7.5 Ce), respectively, whereas in the low-density state, the coordination numbers are 10.9 (3.1 Al + 7.8 Ce) for Al and 14.1 (5.7 Al + 8.4 Ce) for Ce. The single-peak Ce–Ce bond length distribution in the low-density state (see Fig. 3b), in particular, is replaced by approximately 3.5 Ce atoms in the inner shell (<3.1 Å) and 4.0 Ce atoms in the outer shell for the high-density state. These structural differences are responsible for the feature changes seen in the XRD patterns.

In Supplementary Information, Fig. S6, we also show that all of the details in the experimental structure factor at 19.8 GPa (point C in Fig. 2) do not agree with those simulated assuming *f*-electron localization, but can be fully accounted for in a simulation of the high-density glass. This match further rules out crystallization as a cause for the changes in the XRD features, as all the distribution functions in Supplementary Information, Fig. S6 clearly indicate that the system is fully amorphous. Minor crystallization below the detection limit, if any at all in the experimental samples, cannot explain the large density increase in Fig. 2.

The *f*-electron delocalization promotes the low-lying *f*-electrons to close to the Fermi level (E_F), as shown in the electron density of states shown in Fig. 4a,b. For crystalline Ce, it is believed[21] that the 4*f*-electron localization and screening effects are responsible for the polymorphism. Under pressure, the 4*f*-electrons become more itinerant and participate in bonding as the atomic overlap is increased[8–10]. The transition of Ce crystal from one face-centred-cubic state to another thus exhibits a large volume collapse (~15% at 0.8 GPa at room temperature). In our $Ce_{55}Al_{45}$ glass, the electron density isosurface contours from our *ab initio* calculations for the two amorphous states are compared in Fig. 4c,d. It can be seen that pressure induces closer Ce–Ce approaches/interactions and *f*-electron delocalization, which enhances the electronic bonding, resulting in reduced Ce–Ce interatomic distances (that is, pronounced Ce–Ce bond shortening). The emergence of shortened Ce–Ce bonds is clearly seen in the pair distribution function in Fig. 3d.

Pressure-induced qualitative changes in electronic interactions resulting in bond shortening seem to be the origin of the large volume reduction seen in our experiments, see Fig. 2. This mechanism involves the changes in electronic bonding between atoms, rather than the changes in atomic coordination alone or the directionality of the covalent bonds. Here, both amorphous states are metallic (Fig. 4), and the polyamorphic transition is abrupt during decomposition (Fig. 2). The somewhat sluggish transition during compression is probably due to the presence of Al atoms, which renders the Ce–Ce approach difficult, and the inherent variations of local atomic environments in the glass. Although Ce is archetypal of localization–delocalization phenomenon and a prominent example showing the associated drastic density changes, it is by no means the only one. Electron evolution, for example, from a more localized state to a more itinerant one as a function of a thermodynamic parameter such as pressure, and the multiple- or mixed-valence behaviour, are not uncommon for metallic elements[8,9,22,23]. Dramatic bond shortening has been noticed in

©2007 Nature Publishing Group

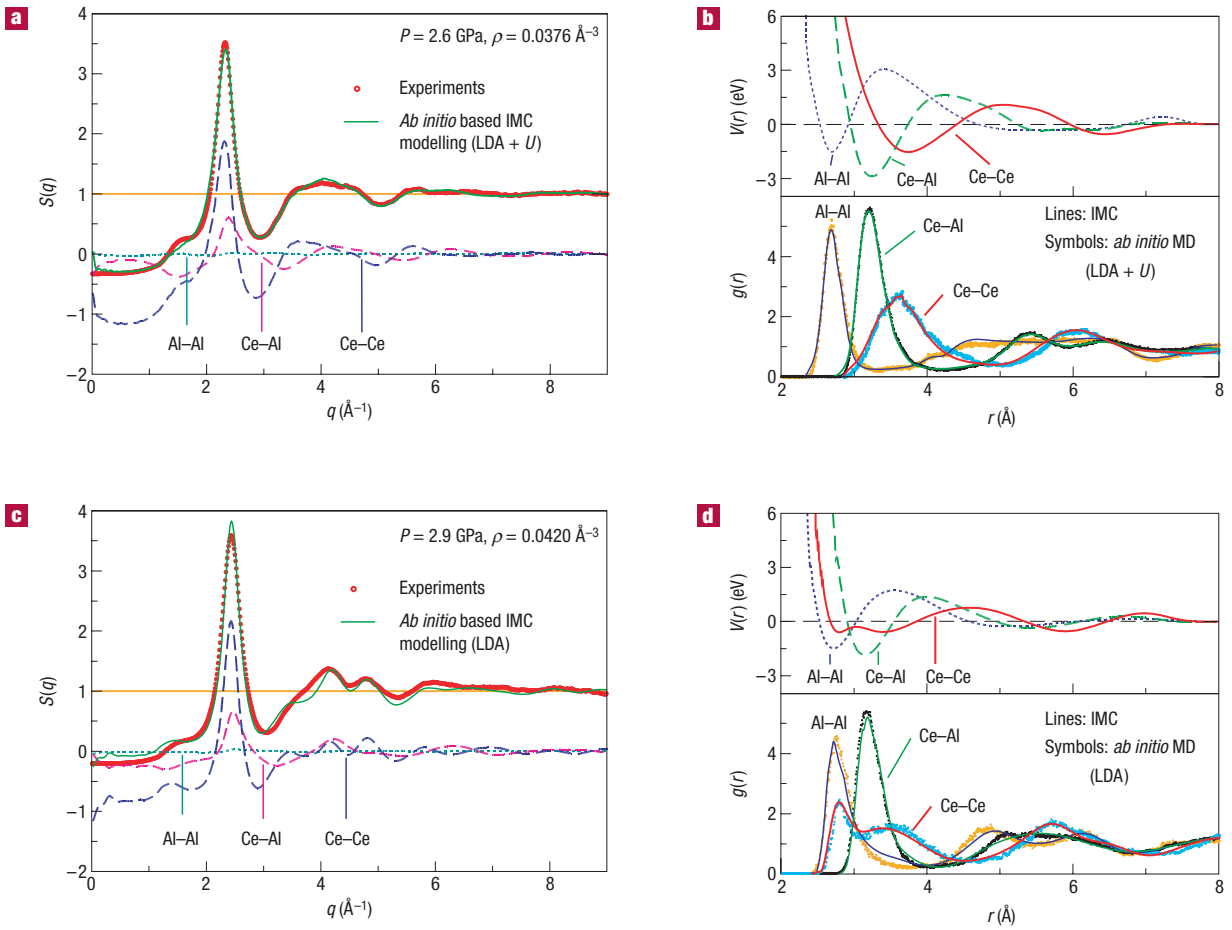

Figure 3 Comparison of the structure factors for the two amorphous polymorphs of $Ce_{55}Al_{45}$ at comparable pressures. a,**b**, For the low-density glass, during the initial compression stage before transforming to the high-density state. **c**,**d**, For the high-density amorphous phase retained to a relatively low pressure. The structure factors calculated for the two distinct amorphous states are also included in **a** and **c** for comparison (see the Methods section). The total structure factors comprise the contributions from the Faber–Ziman partial structure factors, and the weighted Faber–Ziman structure factors are indicated by dashed lines. The effective pair potentials $V(r)$ derived using the IMC method (see the Methods section) on the basis of the *ab initio* results, and the pair distribution functions $g(r)$ derived from the IMC models, are provided for the two glass phases, in **b** and **d**, respectively.

Al-based MGs, although its electronic origin and the control of its development are yet to be established. For a number of amorphous metals and their alloys, anomalies have been observed in the liquid state and in their melting/freezing behaviour[23,24]. Therefore, high-density amorphous metals may exist for many MGs and their parent metallic liquids. Phase changes associated with metallic polyamorphism are thus possible in general, when the underlying electronic interactions are altered abruptly under certain processing or external forcing conditions, opening up a new area for future research. The volume collapse and Kondo transition associated with f-electron delocalization in strongly correlated systems is also a subject of considerable interest in the condensed-matter physics community[8–10], and remains to be systematically explored in amorphous alloys.

METHODS

Metallic glass $Ce_{55}Al_{45}$ (ribbons, ~30 μm thick, 5 mm wide) was prepared using the single-roller melt-spinning technique. Its composition was confirmed to be accurate within an error margin of 2.0% using energy-dispersive X-ray spectroscopy. Using the Archimedes principle, the density of the sample under ambient pressure is measured to be 5.287 g cm^{-3} (~0.0357 ± 0.0003 Å^{-3} in number density, corresponding to the specific volume in Fig. 2).

Three of the four sets of *in situ* high-pressure XRD experiments were carried out at the ID-B station of the High Pressure Collaborative Access Team (HPCAT), Advanced Photon Source (APS), Argonne National Laboratory. Pressure in the range of 0–32 GPa was applied to the sample using a diamond anvil cell (DAC, see the schematic diagram in Supplementary Information, Fig. S7). The pressure was measured using the ruby fluorescence method. The time interval between each pressure adjustment was ~45 min. Monochromatic synchrotron X-ray beams were microfocused to ~15 μm in diameter. The energies of the incident beam were 28.27, 30.87 and 31.89 keV respectively, allowing reliable diffraction patterns to be taken up to a scattering vector of $q \sim 6.0$ Å^{-1} in the presence of the DAC. To resolve the structural evolution more precisely, focused high-energy (100.23 keV, $\lambda = 0.1239$ Å) XRD at the 1-ID beamline, APS, was used to collect the fourth set of diffraction data, reaching a much larger momentum transfer q (~18 Å^{-1}) even at the high pressures in the DAC.

Diffraction patterns were recorded on the MAR345 image plate at HPCAT and the GE Angio amorphous Si detector at 1-ID and were then integrated using the FIT2D program. Taking into account the background subtraction, absorption correction, multiple-scattering correction and incoherent Compton scattering, a new least-squares method was used to obtain the total structure factors of the sample at each pressure (see Supplementary Information, Fig. S8).

©2007 Nature Publishing Group

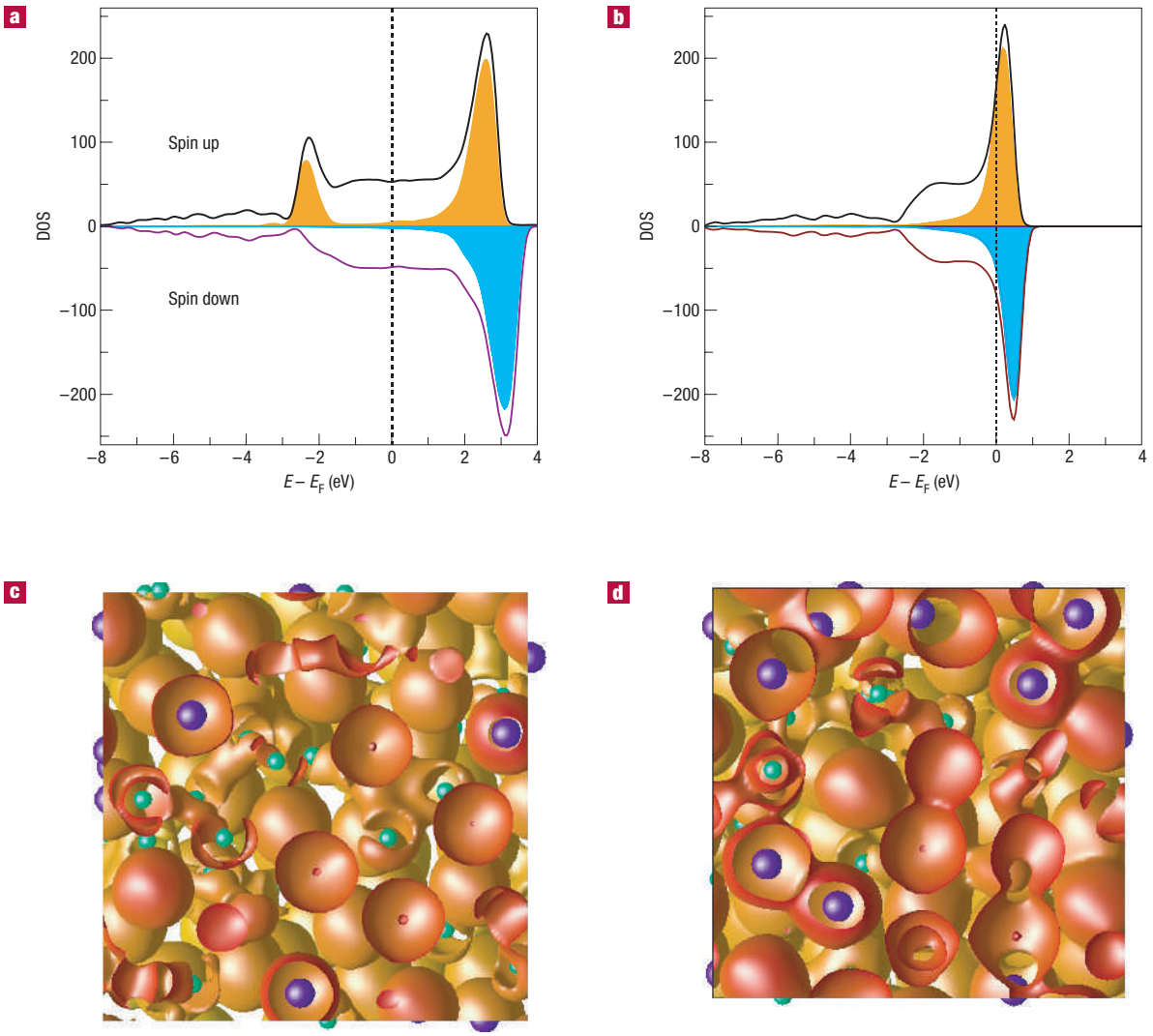

Figure 4 Comparison of spin-resolved electron density of states (DOS), obtained for the two amorphous $Ce_{55}Al_{45}$ phases. a, The LDA + *U* calculation of the low-density glass at 2.5 GPa, where the low-lying *f* band (colour shaded areas represent *f* electron states) indicates that the *f*-electrons are localized. **b**, The LDA calculation of the high-density glass at 2.5 GPa, where the *f*-electrons become itinerant, participating in bonding. **c**,**d**, The two-dimensional projections of the 3D isosurfaces of the electron charge density for the two calculations (LDA + *U* versus LDA) in **a**,**b**. The strong bonding between Ce–Ce (with much shortened bond lengths) is apparent in the *f*-electron delocalized glass (LDA calculation, **d**). The blue and green spheres mark the centres of the Ce and Al atoms, respectively.

Reproducibility was confirmed with multiple runs/samples (see Supplementary Information, Fig. S7).

First-principles calculations on the basis of the density functional theory were used, via *ab initio* molecular dynamics (MD) simulations as implemented in the Vienna Ab-initio Simulation Package[25] 'VASP', to achieve the atomic configurations of the quenched glass, as well as its EOS. To model the dual valance states of Ce (at ambient pressure, Ce remains purely trivalent in Ce–Al amorphous alloys[26]; mixed valences, such as trivalent and tetravalent Ce, are also of interest here), the amorphous Ce–Al was treated in two ways: the LDA was assumed to describe the *f*-delocalized Ce, whereas the Hubbard *U* term was added (that is, LDA + *U*) to model the *f*-localized Ce[10]. For the latter calculation, Dudarev's approach[27] was adopted, with the Hubbard *U* parameter empirically set to be 5.6 eV. These *ab initio* models are used to represent the two extremes of the *f*-electron behaviour. Projected augmented planewaves with the LDA have been adopted[28,29].

Canonical NVT (constant number, volume, temperature) ensembles containing 100 atoms with a periodic boundary condition were melted and equilibrated at 1,500 K for 2,000 time steps (each time step represents 5 fs). The temperature was controlled with a Nose–Hoover thermostat. The initial density of the high-*T* liquid was adjusted to have a zero pressure on its inherent structure[30]. The quenching rate used to obtain the metallic glass was 20 K per 100 time steps. The *ab initio* MD was carried out only on the Γ point, but for the accurate electronic structure calculation (see Fig. 4), the Brillouin zone was sampled with 3 × 3 × 3 Monkhorst–Pack *k*-point grids. A gaussian method was used for the Fermi-surface smearing, with a width of 0.15 eV.

At each volume (density) perturbation, the inherent structure was located using the conjugated gradient method, and the pressure was calculated. The inherent structure[30] corresponds to the minimum energy of the basin of attraction, and is mechanically stable. By using this mechanical compression method, the *P*–*V* curve (EOS) was obtained. Meanwhile, *ab initio* MD of the inherent structures yields the ideal pair distribution functions at the designated pressures, which are used for further structural modelling.

Larger systems with 100,000 atoms were generated using the IMC method[20], for calculation of structure factors that can be directly compared with experiments. The newly generated atomic configurations have the same pair distribution functions as that obtained from the *ab initio* MD (see Supplementary Information, Fig. S5). These simulated systems were also used to determine the density of experimental samples at different pressures: the size of the simulation box was adjusted until the closest match (primarily the first peak) between the experimental structure factor and the simulated one was

©2007 Nature Publishing Group

found. When a best match between the theoretical and experimental structure factor was desired, such as in Supplementary Information, Fig. S6, the empirical potential structure refinement technique was applied[31]. Geometrical analysis on the atomic configurations, using the Voronoi tessellation method[32], yields information about the atomic packing, such as the bond lengths, atomic coordination numbers, and bond-angle distribution.

Received 31 October 2006; accepted 19 December 2006; published 18 February 2007.

References

1. McMillan, P. F. Polyamorphic transformations in liquids and glasses. *J. Mater. Chem.* **14**, 1506–1512 (2004).
2. Mishima, O., Calvert, L. D. & Whalley, E. An apparently first-order transition between two amorphous phases of ice induced by pressure. *Nature* **314**, 76–78 (1985).
3. Meade, C., Hemley, R. J. & Mao, H. K. High-pressure x-ray-diffraction of SiO_2 glass. *Phys. Rev. Lett.* **69**, 1387–1390 (1992).
4. Morishita, T. High density amorphous form and polyamorphic transformations of silicon. *Phys. Rev. Lett.* **93**, 055503 (2004).
5. McMillan, P. F. *et al.* A density-driven phase transition between semiconducting and metallic polyamorphs of silicon. *Nature Mater.* **4**, 680–684 (2005).
6. Katayama, Y. *et al.* A first-order liquid–liquid phase transition in phosphorus. *Nature* **403**, 170–173 (2000).
7. Sen, S., Gaudio, S., Aitken, B. G. & Lesher, C. E. A pressure-induced first-order polyamorphic transition in a chalcogenide glass at ambient temperature. *Phys. Rev. Lett.* **97**, 025504 (2006).
8. Soderlind, P. Theory of the crystal structures of cerium and the light actinides. *Adv. Phys.* **47**, 959 (1998).
9. Svane, A. *et al.* Self-interaction-corrected local-spin-density calculations for rare earth materials. *Int. J. Quant. Chem.* **77**, 799–813 (2000).
10. Shick, A. B., Pickett, W. E. & Liechtenstein, A. I. Ground and metastable states in gamma-Ce from correlated band theory. *J. Electron Spectrosc. Relat. Phenom.* **114**, 753–758 (2001).
11. Poole, P. H. *et al.* Polymorphic phase transitions in liquids and glasses. *Science* **275**, 322–323 (1997).
12. O'Keeffe, M. & Navrotski, A. (eds) in *Structure and Bonding in Crystals* (Academic, New York, 1981).
13. Lacks, D. J. First-order amorphous-amorphous transformation in silica. *Phys. Rev. Lett.* **84**, 4629–4632 (2000).
14. Angell, C. A. Formation of glasses from liquids and biopolymers. *Science* **267**, 1924 (1995).
15. Greer, A. L. Metallic glasses. *Science* **267**, 1947 (1995).
16. Sheng, H. W. *et al.* Pressure tunes atomic packing in metallic glass. *Appl. Phys. Lett.* **88**, 171906 (2006).
17. Jiang, J. Z., Gerward, L. & Olsen, J. S. Comment on "Reversible phase transition between amorphous and crystalline in $Zr_{41.2}Ti_{13.8}Cu_{12.5}Ni_{10}Be_{22.5}$ under high pressure at room temperature". *Appl. Phys. Lett.* **80**, 3015–3016 (2002).
18. Gschneider, K. A. Jr & Eyring, L. R. (eds) in *Handbook on the Physics and Chemistry of Rare Earths* (North-Holland, Amsterdam, 1978).
19. Jayaraman, A. Fusion curve of cerium to 70 kilobar and phenomena associated with supercritical behavior of fcc cerium. *Phys. Rev. A* **137**, 179–182 (1965).
20. Almarza, N. G. & Lomba, E. Determination of the interaction potential from the pair distribution function: An inverse Monte Carlo technique. *Phys. Rev. E* **68**, 011202 (2003).
21. Johansson, B. Alpha-gamma transition in Cerium is a Mott transition. *Phil. Mag.* **30**, 69–482 (1974).
22. Maddox, B. R. *et al.* 4*f* delocalization in Gd: Inelastic X-ray scattering at ultrahigh pressure. *Phys. Rev. Lett.* **96**, 215701 (2006).
23. Falconi, S., Lundegaard, L. F., Hejny, C. & McMahon, M. I. X-ray diffraction study of liquid Cs up to 9.8 GPa. *Phys. Rev. Lett.* **94**, 125507 (2005).
24. Errandonea, D., Boehler, R. & Ross, M. Melting of the rare earth metals and *f*-electron delocalization. *Phys. Rev. Lett.* **85**, 3444–3447 (2000).
25. Kresse, G. & Furthmüller, J. Efficiency of ab-initio total energy calculations for metals and semiconductors using a plane-wave basis set. *Comput. Mater. Sci.* **6**, 15–50 (1996).
26. Malterre, D., Krill, G., Durand, J., Marchal, G. & Ravet, M. F. Electronic configuration of Ce in amorphous alloys investigated by x-ray absorption spectroscopy. *Phys. Rev. B* **34**, 2176–2181 (1986).
27. Dudarev, L. *et al.* Electron-energy-loss spectra and the structural An LSDA + U study stability of nickel oxide. *Phys. Rev. B* **57**, 1505 (1998).
28. Blöchl, P. E. Projector augmented-wave method. *Phys. Rev. B* **50**, 17953–17979 (1994).
29. Kresse, G. & Joubert, D. From ultrasoft pseudopotentials to the projector augmented-wave method. *Phys. Rev. B* **59**, 1758–1775 (1999).
30. Stillinger, F. H. & Weber, T. A. Packing structures and transitions in liquids and solids. *Science* **225**, 983–989 (1984).
31. Soper, A. K. Partial structure factors from disordered materials diffraction data: An approach using empirical potential structure refinement. *Phys. Rev. B* **72**, 104204 (2005).
32. Sheng, H. W., Luo, W. K., Alamgir, F. M., Bai, J. M. & Ma, E. Atomic packing and short-to-medium range in metallic glasses. *Nature* **439**, 419–425 (2006).

Acknowledgements

This work was supported by US Department of Energy, Office of Science, Basic Energy Sciences, Division of Materials Sciences and Engineering, under contract No. DE-FG02-03ER46056. The APS and HPCAT facilities were supported by DOE-BES, DOE-NNSA (CDAC), NSF, DOD-TACOM and the W. M. Keck Foundation.
Correspondence and requests for materials should be addressed to H.W.S. or E.M.
Supplementary Information accompanies this paper on www.nature.com/naturematerials.

Competing financial interests

The authors declare that they have no competing financial interests.

Reprints and permission information is available online at http://npg.nature.com/reprintsandpermissions/

©2007 Nature Publishing Group